Evaluation of transient turbulent flow fields using digital cinematographic particle image velocimetry

S. Y. Son, K. D. Kihm

Abstract This paper describes an experimental development for temporal and spatial reconstruction of continuously varying flow fields by means of digital cinematographic particle image velocimetry (PIV). The system uses a copper-vapor laser illumination synchronized with a high-speed camera, and continuously samples at 250 fps to measure transient and non-periodic turbulent flows with relatively low frequencies, i.e., the surf zone turbulence produced by depth-limited wave break in a long laboratory flume. The use of the developed PIV system comprehensively records the temporal development of both phase-averaged and instantaneous turbulent vortex flows descended from the breaking waves to the bottom. Also, the measured power spectra show harmonic frequencies, ranging from the orbital frequency of 0.5 Hz up to the order of 5 Hz, and the well-known −5/3 dependence upon the turbulence fluctuation frequencies thereafter.

1
Introduction

The particle image velocimetry (PIV) technique has become a fast-growing attraction in measuring flow velocity fields, primarily due to its breakthrough advantage of whole-field mapping capability over the traditional single-point measurement probes. Extensive bibliography of the literature on PIV development is available from several review publications (e.g., Adrian 1996; Raffel et al. 1998).

The recent development of a cross-correlation CCD camera, synchronized with pulsed Nd:YAG laser illumination, allows sufficiently fast recording of two consecutively time-tagged images, which alleviates the flow direction ambiguities occurring in the case of auto-correlation of superimposed images on a single frame (Adrian 1986). This also eliminates the image-biasing problem caused by the image shift when using a rotating

S. Y. Son, K. D. Kihm (✉)
Department of Mechanical Engineering
Texas A and M University
College Station, TX 77843-3123, USA

mirror arrangement (Raffel and Kompenhans 1995; Lee et al. 1996). In addition, the unprecedented advancement of computer technology makes it possible to handle and process excessive amounts of digitized data of literally thousands of PIV images.

However, the relatively slow repetition rates of conventional pulsed Nd:YAG lasers of the order of 10 Hz creates a challenge in measuring turbulent flows. According to the Nyquist theorem (Bradshaw 1971), the sampling rate must be at least twice as fast as the smallest data periodicity to avoid problems of aliasing. Besides, such intermittently sampled data can statistically represent the flow characteristics only if the flow remains "ensemble-averaged" steady, i.e., stationary turbulent flows (Westerweel et al. 1997; Son et al. 1999). For the limited case of a transient but highly periodic flow, the phase-averaged intermittent sampling can estimate turbulence properties to some extent (Raffel et al. 1996).

For increased sampling frequencies, a number of attempts have been made to convert a continuous wave (CW) laser illumination into pulses at sufficiently high repetition rates using a mechanical chopping device. The use of a mechanical shutter, however, chops out a significant portion of the CW light energy, and only a small portion of the total power is used to image the view. This results in degraded signal-to-noise ratios, which are increasingly worse for faster shutter speeds. The use of a mechanical shutter has been mainly used for relatively slow transient flows, i.e., laminar flows (Hassan et al. 1993; Oakley et al. 1997; Lyn 1997; Tokuhiro et al. 1999). Merzkirch et al. (1994) showed the feasibility of cinematographic PIV using a video recorder operating at 40 fps. Their recording period was extended up to 60 min to image slowly time-dependent natural convection flows with a CW He–Ne laser sheet illumination.

Lawson et al. (1999) used a rotating mirror to generate 200 Hz pulsed illumination from a CW 4-W argon-ion laser. The recording hardware, using a 35 mm camera, was limited to four consecutive images at a time, superimposed on a single film plate. Using this technique, an instantaneous flow field around a collapsed bubble was recorded at a certain time delay after the initial rupture of the bubble. This technique is essentially analogous to the use of a Nd:YAG laser system containing four resonators, instead of two, and therefore shares the same limitation of intermittent sampling as the conventional PIV system in measuring transient flow turbulence.

A rotating drum camera has been used to image dynamic flow processes under a compression stroke of a

piston-cylinder configuration (Hartmann et al. 1996). Based on our literature survey, this work was the first attempt to use a copper-vapor laser synchronized with the image recording at high temporal resolution. Because of the hardware limitation of the drum camera, however, only a limited number of consecutive images (a total of 40–70 frames) were recorded for a very short time period, of the order of 10 ms. While the technique allowed instantaneous flow fields and their short-time ensemble averaged velocity fields, temporally comprehensive full-field turbulent flow mapping was not possible because of an insufficient number of samplings.

Liu et al. (1999) used a copper-vapor PIV system to study the sub-grid scale isotropic turbulence generated with a nearly periodic flow environment. Their use of a 35-mm film movie camera allowed extremely high vector resolution per single field-of-view. The image shifting scheme was used to solve the directional ambiguity and auto-correlation was used to calculate the flow vectors. The recording rate was fixed at 33 fps as the tested flow oscillates with relatively low fluctuation frequencies.

The assumption for the intermittent samplings most often fails to measure properties for transient and non-periodic turbulent flows. The purpose of this work is to implement a digital cinematographic PIV system that can sample images at higher frame rates than the flow fluctuation frequencies for a sufficient period of time, in order to accurately map transient, non-periodic turbulent flow characteristics, spatially as well as temporally. The PIV system developed has been tested to measure the intermittent and non-periodic surf-zone turbulent vortex flows descending from the breaking surface waves (Fig. 1).

Turbulence is one of the most significant phenomena that fundamentally characterize the underlying surf-zone flow field below trough level, and knowledge of turbulent vortex development is crucial to the understanding of processes of practical importance such as sediment transport and shore erosion. The investigation of the turbulent flow field, particularly near the bottom, including the development of obliquely descending eddies after the breaking wave is necessary for comprehensive understanding of the surf-zone wave dynamics. Although there have been studies using point measurements (e.g., Nadaoka et al. 1989), based on the authors' survey, no full-field quantitative description of the turbulent flows of the descending eddies has been published.

PIV has been used in the flow study beneath the breaking waves to some extent. Lin and Rockwell (1995) examined a quasi-steady breaking wave using a rotating mirror PIV system with a film camera and an argon-ion CW laser. They showed the patterns of instantaneous vorticity and velocity fields beneath the breaking wave. Extensive PIV studies on the breaking waves were conducted at Edinburgh University (Gray et al. 1991). A PIV system using a scanning beam illumination method was applied to examine the breaking wave kinematics (She et al. 1997). These existing studies have been mainly focused on the region just beneath the breaking waves, and their measurements were made mainly for vertical measurement planes. Extended measurements to the region near the bottom will be necessary to further understand the flow beneath breaking waves and the successive vortex shedding.

2
Experimental setup

The experimental setup (Fig. 2) consists of the high-speed cinematographic PIV system and a wave generation system. Both systems are controlled and synchronized by digital triggering signals from a PC with a National Instrument data acquisition board. The cinematographic sampling allows improved vector validation by temporal post-processing, in addition to the conventional spatial post-processing.

2.1
High-speed digital cinematographic PIV system

The PIV system consists of a 20-W nominal output copper-vapor laser Model LS-20 from Oxford Lasers. The output spectrum is double-peaked at 510.6 nm (green) and 578.2 nm (yellow) with an intensity ratio of approximately 2:1. The inherently high lasing efficiency of the system, involved in the transitions in free uncharged metal vapor atoms, allows a high repetition rate of up to 10,000 Hz. The individual pulse energy is higher than 4 mJ with the burst mode (a batch of several hundred pulses for one time operation) at a pulse duration of approximately 27 ns, equivalent to the peak power of 300 kW. The output beam of 25 mm diameter is close to the "top hat" profile in the near field. A series of spherical and cylindrical lenses collimates the beam to a 2-mm-thick light sheet.

The Phantom Model V3.0 high-speed video camera records images in synchronization with the laser pulses. The camera itself has an 8-bit resolution and a 256-Mbyte direct image memory (DIM), which allows continuous recording of 1,024 images at 512×512 pixel resolution. The 512×512 imager CCD chip has dimensions of 9.22 mm $\times$ 9.22 mm and the size of each pixel is
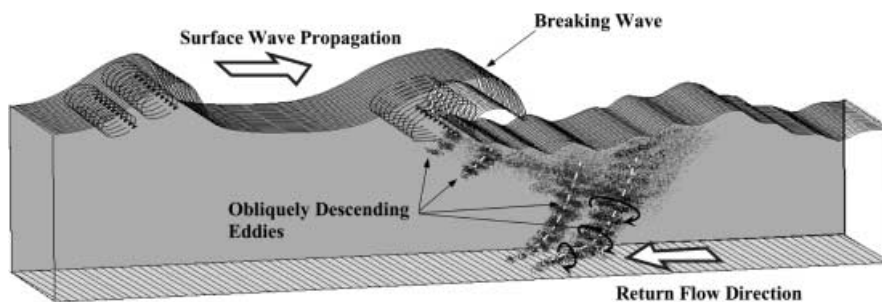

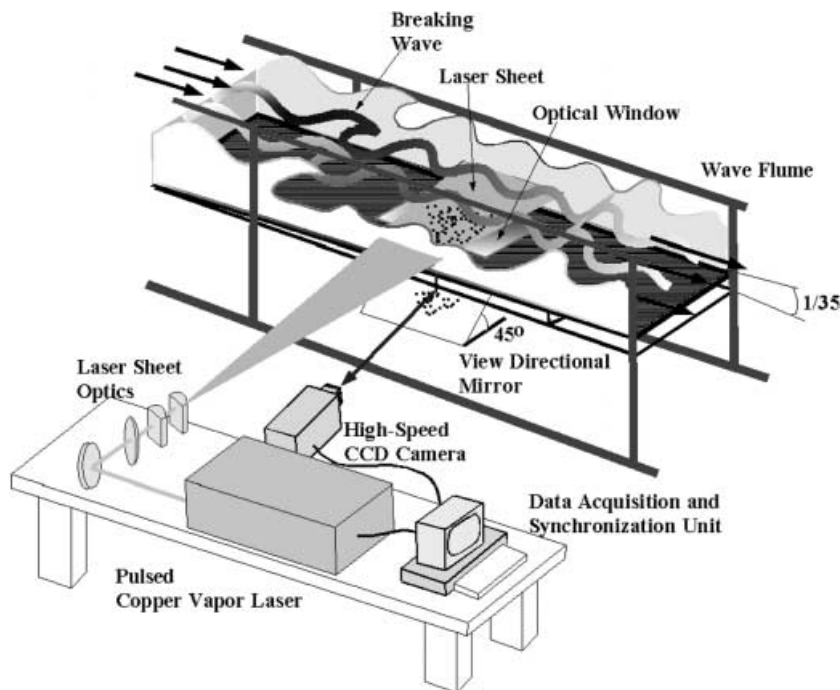**Fig. 1.** A schematic illustration of obliquely descending eddies from the breaking surface waves

Fig. 2. Cinematographic PIV system config-
uration with the wave flume

$d_r = 18 \times 18$ μm. The capture rate ranges from 1 to 576 fps at the full resolution, and can be extended up to 3,000 fps at a reduced pixel resolution. For the present experiment, the 250 fps capture rate with full resolution was used, based on the preliminary evidence obtained by using a single-probe LDV measurement, showing that the fluctuating time scale usually spans longer than 10 ms under similar flow conditions (Nadaoka et al. 1989). The DIM allows 1,024 sequential images to be captured for 4 s during two consecutive 2-s period waves. Then, the captured images are stored in CD-recordable disks for later PIV analysis. The field-of-view of the PIV image was set as ($l_x = 70.7$ mm) $\times$ ($l_y = 70.7$ mm) using a Nikon 105-mm manual lens ($f^\# = 4.0$) at its magnification $M_o = 0.133$.

The standard cross-correlation scheme based on fast Fourier transform (FFT), developed by LaVision, Inc., was used to process the PIV images to obtain raw vector fields. The scheme also implements the multipass interrogation process with an adaptive window offset algorithm. Using the window offset significantly increases the signal-to-noise ratio for PIV measurement. The window offset also improves the spatial resolution by reducing the effective interrogation window size (Westerweel et al 1997). The first-pass cross-correlation is calculated for a 64×64-pixel interrogation window by FFT without window offset, and then the interrogation window is divided into four sub-areas 32×32 pixel for the second-pass calculation. The estimated displacement value from the first pass is used as the window offset value for the second 32×32-pixel interrogation window calculation.

The selection of the window size (32×32 pixel square window of approximately 4.42 mm) was based on the statistical assessment of a minimum of five image pairs for single vector detection. The particle image pair density affects both the probabilities of valid displacement detection and the measurement uncertainties. Keane and

Adrian (1992) used the computer-synthesized image data to assert that at least three particle image pairs per interrogation showed good matches with the simulation data. Additional consideration for the window size selection was based on the maximum particle displacement during the sampling period, $x_{pmax} = 1.2$ mm for $u_{max} = 0.3$ m/s $\times \Delta t = 0.004$ s. This maximum particle displacement is equal to approximately 28% of the linear dimension of the interrogation window and equivalent to nine pixels in the imaging plane. For the current field-of-view 70.7 mm square, a vector matrix of 32×32 elements is available when the interrogation windows are overlapped by 50%.

2.2
Dynamic velocity range

The dynamic velocity range (DVR) specifies the range of velocity variation over which measurements could be made. The maximum velocity in the tested surf-zone vortex flow field was found to be $u_{max} = 0.3$ m/s and the minimum resolvable velocity vector magnitude was conservatively estimated, based on the experimental observation, to be $u_{min} = 1.5$ mm/s. Thus, the required DVR for the present study is estimated at 200. The DVR of the assembled PIV system is calculated using the theory developed by Adrian (1997), where DVR is defined as the ratio of the maximum velocity to the minimum resolvable velocity, or equivalently the rms error in the velocity measurement, i.e.,

$$\text{DVR} = \frac{u_{max}}{\sigma_u} = \frac{u_{max}}{\sigma_{\Delta X} M_o^{-1} \Delta t^{-1}} \tag{1}$$

where the image magnification $M_o = 0.133$, and the laser pulse interval $\Delta t = 0.004$ s. The rms error of the displacement on the pixel plane $\sigma_{\Delta x}$ is asserted as 4% of the recorded image diameter, i.e.,
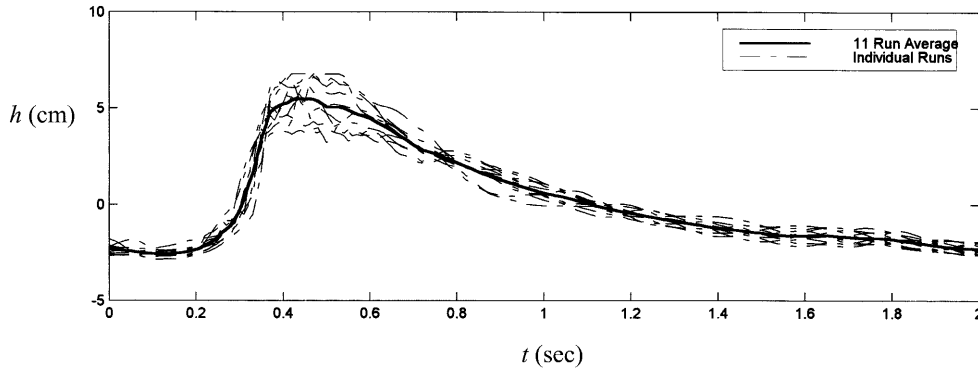
Fig. 3. Temporal history of surface elevation $h(t)$ measured by a wave gauge

$$\sigma_{\Delta X} = 0.04\left(d_e^2 + d_r^2\right)^{1/2} \qquad (2)$$

where $d_r = 18$ μm represents the resolution of the recording medium that is taken to be equivalent to the pixel size, and d_e is the diameter of the particle image prior to being recorded on the pixel plane.

Assuming that the particle image is diffraction limited and its image intensity is Gaussian, the diameter of the diffracted image of the particle is expressed as (Goodman 1996):

$$d_e^2 = M_o^2 d_p^2 + \left[2.44(1 + M_o)f^{\#}\lambda\right]^2 \qquad (3)$$

where the seeding particle diameter $d_p = 14$ μm MMD (silver-coated hollow glass spheres of density 1.3 g/cm^3), the f number of the imaging lens $f^{\#} = 4.0$, and the laser wavelength λ_l is taken as 530 nm. Thus, the recorded image diameter $\left(d_e^2 + d_r^2\right)^{1/2}$ is calculated to be 19.0 μm, occupying a little more than 1 pixel. Raffel et al. (1998) estimated an optimum particle image diameter, for minimum uncertainties, as 1.5 pixels by using an artificially generated PIV data. Substituting Eq. (3) into Eq. (2) gives $\sigma_{\Delta x} = 0.76$ μm, and subsequently, the rms velocity measurement error $\sigma_u = 1.46$ mm/s, and Eq. (1) gives DVR = 205. With the given estimation, the calculated DVR is shown to be comparable with the required value of 200.

2.3
Hydrodynamic wave generation system
The wave flume (Fig. 2) consists of a long, glass-walled channel 35 m long (x), 0.9 m wide (y), and 1.2 m high (z), with a still water depth set to 0.5 m. The wave generator, located at one end of the channel, is capable of making repeatable waves of up to 0.25 m in height relative to the still depth. An impermeable, 1:35 slope was located on the opposite side of the wave generator. The PIV imaging plane is located at a depth of 0.14 m in the inclined surf zone of breaking waves, which is approximately 2.0 cm from the inclined bottom on average. The impermeable slope had a 0.4 m × 0.6 m rectangular glass window for optical access for PIV imaging and laser sheet illumination.

The electrical conductance type wave gauge, at 100 Hz fixed sampling rate, measured the free surface elevations during the wave propagation. Figure 3 shows the measured free surface elevation for 11 individual non-breaking waves of constant 0.5 Hz frequency. The wave break is initiated at around $t = 0.5$ s when the wave amplitude is

further increased by the wave generator. While the individual readings show fluctuations, due to wave irregularities and nonlinearities, the phase-averaged data show persistent readings.

3
Results and discussion

3.1
Flow characteristics and visualization
The schematically illustrated unsteady turbulent flow behind the surf-zone wave break (Fig. 1) is visually presented in Fig. 4. In the surf zone, the surface wave crest develops an approximately two-dimensional eddy whose axis is parallel to the lateral y direction. Behind the wave crest, the flow structure is known to quickly develop into three-dimensional eddies stretched obliquely downwards (Nadaoka et al. 1989). The locations and strengths of the obliquely descending eddies are unpredictable and intermittent in both space and time. Thus, while the surface wave propagation is periodic, the turbulent vortex flow near the bottom is non-periodic and transient.

Figure 4a–d shows a sequential development of descending eddies after the wave crest has passed in the surf-zone. Each picture has a field-of-view of approximately 15 cm × 15 cm and the field is illuminated by 4-mm-thick copper-vapor laser sheet. The wave break starts approximately 0.5 s after the wave generation, and the descending eddy is generated soon after the wave breaks (Fig. 4a). The descending eddy develops inclined vortical motion (Fig. 4b) and traps air bubbles that are entrained during the surface wave breaks. The entrapped bubbles descend, together with the descending flow (Fig. 4c). Once the descending eddy reaches a certain depth, the bubbles return to the surface by the overriding buoyant forces; however, the vortex flow, nearly free from bubbles now, continues descending to the bottom (Fig. 4d). The swirling entrainment of sand from the bottom, as shown in Fig. 4c and d, attests that the descending eddy develops three-dimensional vortices near the bottom.

The entrapped air bubbles, several orders of magnitude larger and brighter than the seeding particles, overshadow particle images and obscure them. Indeed, this overshadowing problem by bubble images in two-phase flows still remains to be further investigated by a number of PIV researchers (Hassan et al. 1993; Gui and Mezkirch 1996;
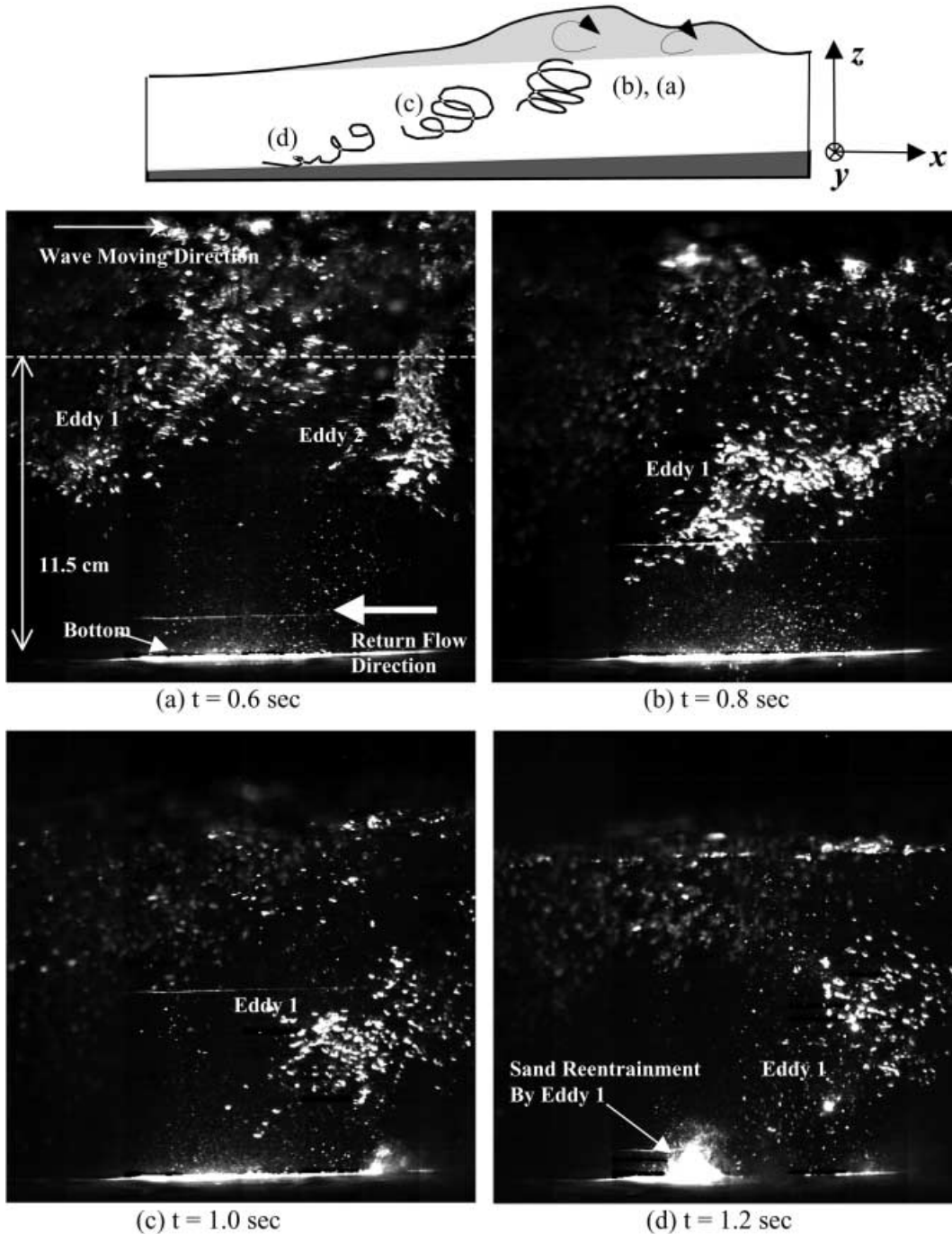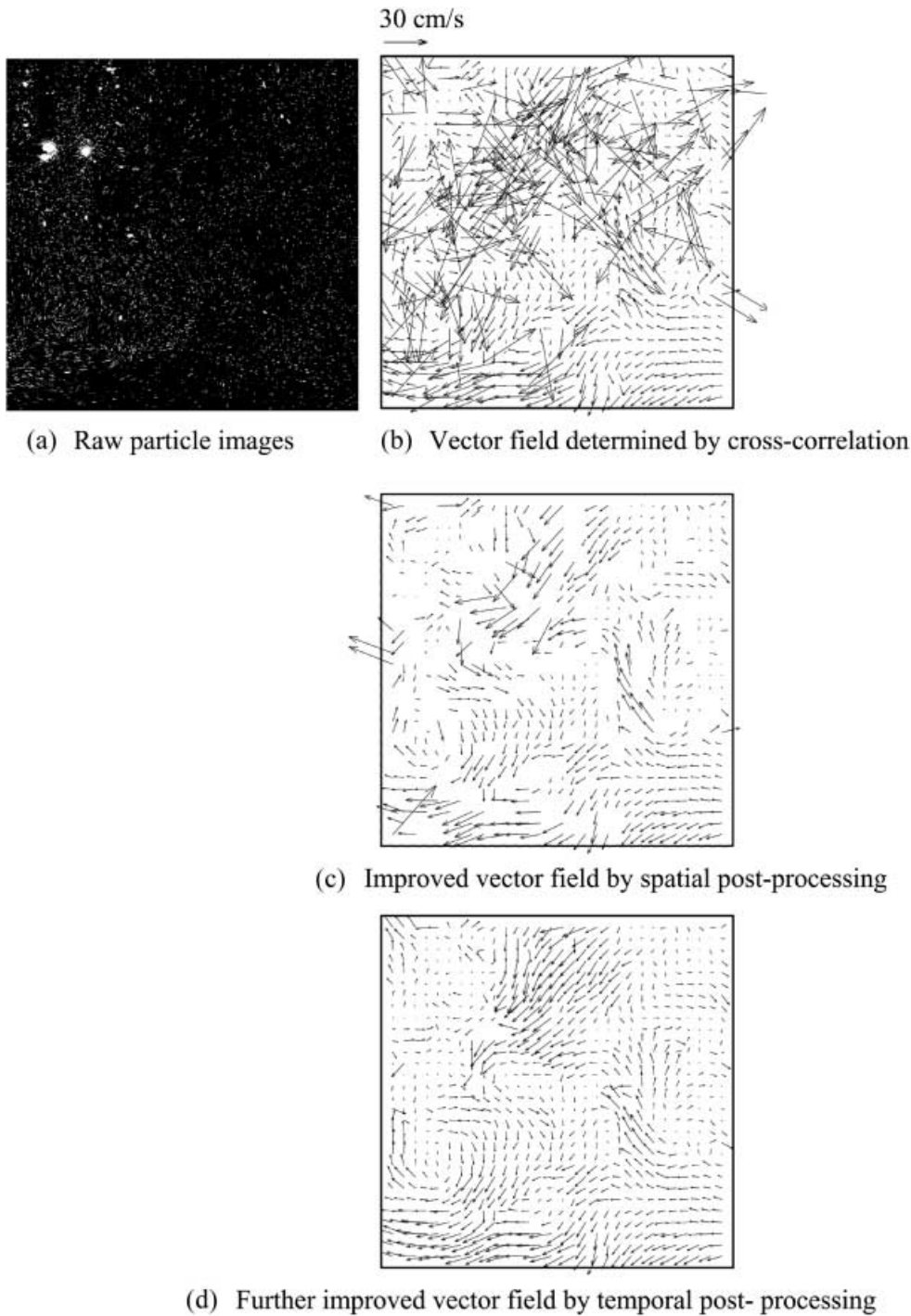
Fig. 4a–d. Laser sheet visualization of descending eddies: **a** $t = 0.6$ s; **b** $t = 0.8$ s; **c** $t = 1.0$ s; **d** $t = 1.2$ s

Lawson et al. 1999). The current PIV measurement was not significantly affected by the overshadowing problem since bubbles hardly reach a depth down to 2 cm from the bottom, where the measurement was made.

3.2
Temporal post-processing
Figure 5a and b shows a raw PIV image and an instantaneous vector field at $t = 0.92$ s when a strong vortex flow is established with a few bubbles presented on the measurement plane, which is one of the worst case examples. The instantaneous vector field is obtained directly from the FFT cross-correlation of two successive bitmap images.

The erroneous vectors are largely a result of the presence of bubbles that are trapped by the descending eddies. The intense and large bubble images blur the surrounding pixels and increase the measurement uncertainties. Another reason for the erroneous vectors may be the three-dimensional nature of the vortex flows that force particles to leave or enter the imaging plane. Also, the erroneous vectors can be generated by the effect of high displacement gradients in an interrogation window. The high shear deforms the fluid during the laser pulse interval, and the high deformation causes the high measurement uncertainty because of in-plane loss of pairs in the correlation analysis (Keane and Adrian 1992; Fincham and Spedding 1997).

(a) Raw particle images

(b) Vector field determined by cross-correlation

(c) Improved vector field by spatial post-processing

(d) Further improved vector field by temporal post- processing

Fig. 5a–d. Progressive improvement of vector field, sampled at $t = 0.92$ s, by spatial and temporal post-processing: **a** raw particle images; **b** vector field determined by cross-correlation; **c** improved vector field by spatial post-processing; **d** further improved vector field by temporal post-processing

The spatially filtered vector field (Fig. 5c) was obtained from the median filtering scheme (Westerweel 1994), where the median of adjacent neighbor vectors, as many as eight, was used as a reference to determine whether the center vector was valid or erroneous. The median filtering effectively eliminates noisy vectors by accepting the center vector only if it falls within a specified range from the median, with the acceptance criteria:

$$[u_{median} - 2.0u_{rms}] \leq u_{center} \leq [u_{median} + 2.0u_{rms}] \quad (4)$$

Otherwise, a new vector corresponding to the next highest correlation peak, on the condition that the new vector

passes the filtering criteria (Eq. 4), replaces the center vector. The weighting factor of 2.0 has been determined based on trial and error for the best validation for most cases. If the new vector does not pass the criteria, the interrogation window is left blank for an additional validation using temporal post-processing.

Non-ideal experimental conditions, such as inhomogeneous seeding, high velocity gradient, high turbulent flow, or inhomogeneous illumination make it impossible to eliminate all the false vectors. The cinematographic sampling allows an additional means of post-processing using temporally neighboring images before and after the
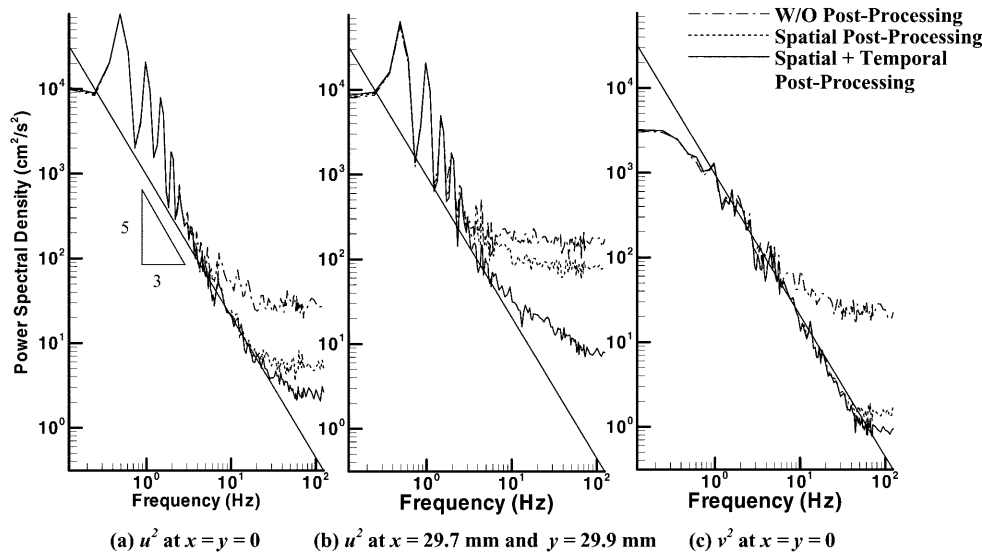
Fig. 6a–c. Power spectral density vs fluctuation frequency: **a** u^2 at $x = y = 0$; **b** u^2 at $x = 29.7$ mm and $y = 29.9$ mm; **c** v^2 at $x = y = 0$

current one. The procedure of the temporal post-processing algorithm is similar to the spatial post-processing in terms of comparisons of neighboring vectors. The selection of the number of temporally neighboring vectors was made so that the time dependence of the flow may not render vectors beyond the criterion range. The acceptance criteria for temporal post-processing is defined as

$$\left| \frac{u_{\text{median}} - u_0}{u_{\text{median}}} \right| \leq \varepsilon \tag{5}$$

where the subscript 0 indicates the present time of recording and the temporal median u_{median} is determined from $(u_{-2} + u_{-1} + u_{+1} + u_{+2})/4$. The subscripts +1 and −1 denote $1 \times \Delta t$ (=4 ms) after, and $1 \times \Delta t$ before the current time, respectively. The criterion ε ranges from 1.5 to 2.0, based on the trial-and-error search, so that it may identify a vector that shows unacceptably large deviation from its temporal neighbors even though it has passed the spatial median filtering.

The temporally false vector, identified from the criterion of Eq. (5), is replaced by the average of two most adjacent vectors, i.e., $u_{\text{new}} = (u_{-1} + u_{+1})/2$. The blank interrogation windows, left from the spatial filtering, are also filled with temporal mean values. The vector field after the combined spatial and temporal post-processing clearly shows more realistic and natural-looking vortex flow patterns (Fig. 5d). The ratio of the vectors subjected to the temporal post-processing varied from 5 to 40% of those already filtered by the spatial post-processing. When no descending bubbles exist, the ratio is as low as 5% and, the ratio can go up to 40% for the case of bubbles presented in the image.

3.3
Power spectral density

One-dimensional power (or energy) spectra of the axial velocity component u are shown for the center location $(x = y = 0)$ of the image plane in Fig. 6a and for a location near the edge at $x = 29.7$ mm, $y = 29.9$ mm in Fig. 6b. The energy spectra were calculated by using the Fourier transformation of the instantaneous velocity $u(t)$ for all 60

waves, i.e., the total of 120 s of temporally recorded data for each specified location. A simple test was conducted to compare the measurements made for 15, 30, and 60 sampling waves, and the resulting phase-average velocities, rms fluctuations, and power spectra showed fairly good consistency for the letter two sampling cases of 30 and 60. Thus, it is believed that the turbulence data obtained from 60 sampling waves are statistically acceptable.

The highest energy peak occurs at 0.5 Hz, equivalent to the orbital wave frequency, and the energy peaks at the harmonic frequencies (1.0 Hz, 1.5 Hz, 2.0 Hz, etc.) are believed to be indicative of wave non-linearity. The subsequent energy cascading down through smaller turbulence length scales follows the well-known "inertial subrange" characteristics of the −5/3 power law (Tennekes and Lumley 1972).

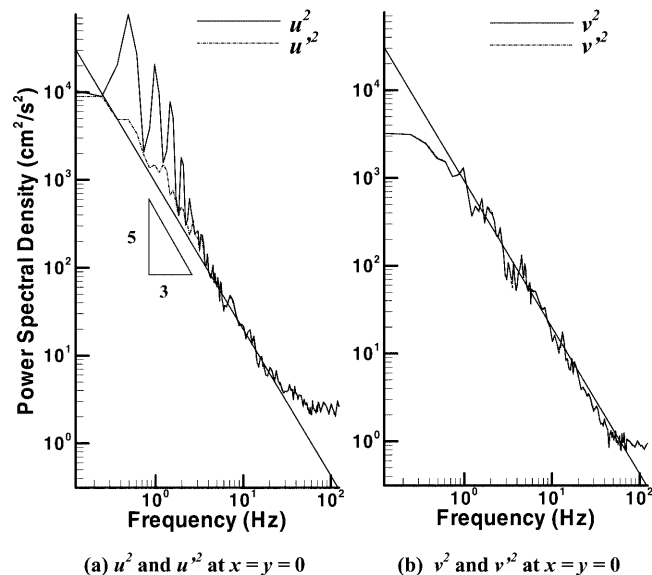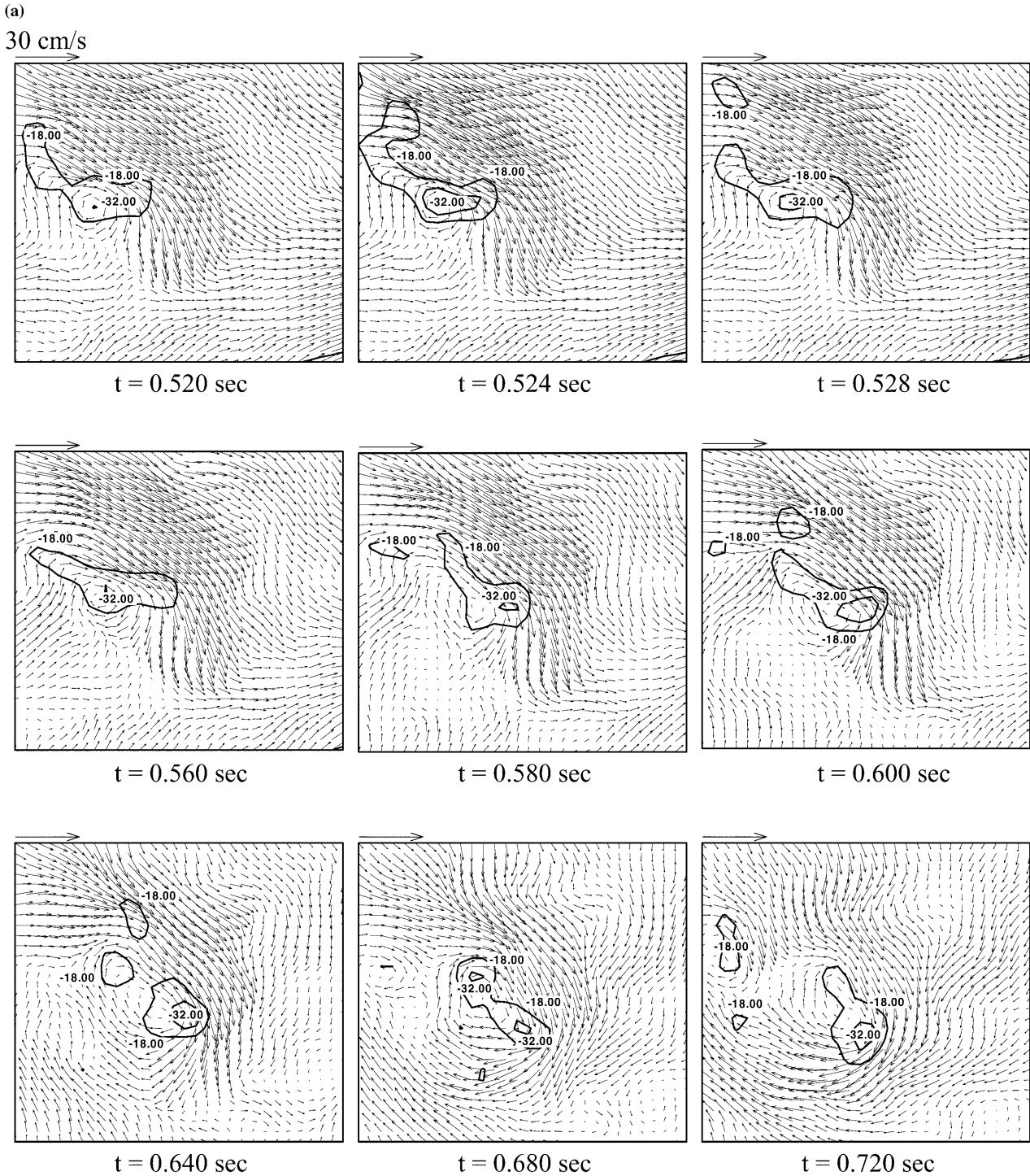The spectra start deviating from the −5/3 power law at a certain frequency and no correlation with the turbu-

Fig. 7a, b. Power spectral density vs fluctuation frequency: **a** u^2 and u'^2 at $x = y = 0$; **b** v^2 and v'^2 at $x = y = 0$

(a)

30 cm/s

t = 0.520 sec

t = 0.524 sec

t = 0.528 sec

t = 0.560 sec

t = 0.580 sec

t = 0.600 sec

t = 0.640 sec

t = 0.680 sec

t = 0.720 sec

Fig. 8. a Temporal development of instantaneous velocity vector field and cut-through vorticity contours at 2 cm above the bottom of the surf zone. **b** Temporal development of phase-averaged velocity vector field from 60 waves and cut-through vorticity contours at 2 cm above the bottom of the surf zone

lence length scale is shown thereafter. Thus, the flattened spectra at the higher frequency are believed to occur due to the imperfect post-processing and other measurement noise. The spatial and temporal post-processing delayed the offset frequencies and extended the valid turbulence measurement range in the spectra. The power spectra obtained with temporally post-processed data follow the −5/3 power line to 30 Hz for the center (Fig. 6a) and

15 Hz for the off-centered location (Fig. 6b), whereas the spatially post-processed data extend merely up to 20 Hz and 5 Hz, respectively. The main reason for the noisier spectra detected at the off-centered location is believed to be the fact that the spatial post-processing using median filter does not effectively work at the border region because of the lack of neighboring vectors there. Although an attempt to use a "flip-filter" can diminish the problem

(b)

30 cm/s

t = 0.520 sec   t = 0.524 sec   t = 0.528 sec

t = 0.560 sec   t = 0.580 sec   t = 0.600 sec

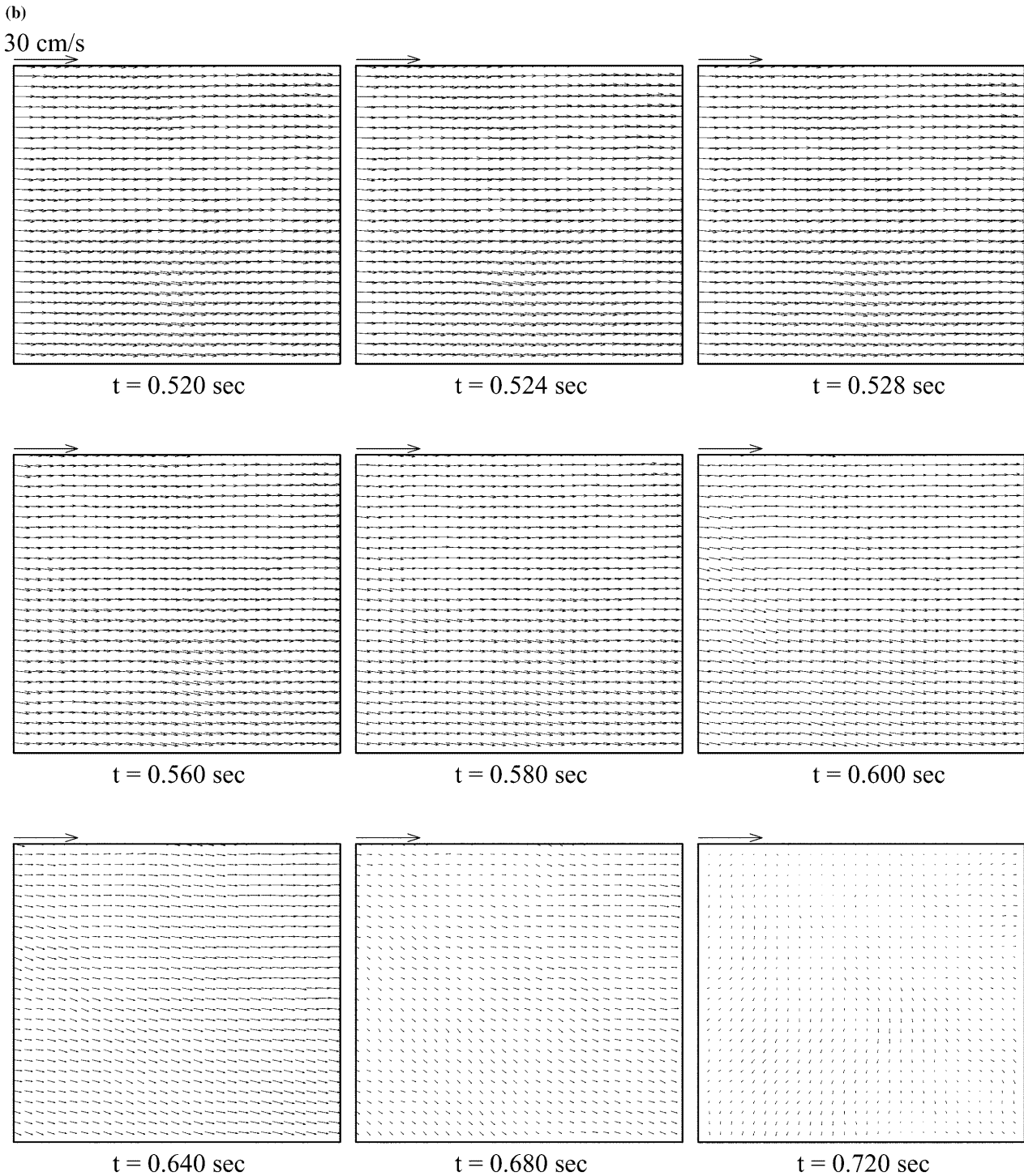t = 0.640 sec   t = 0.680 sec   t = 0.720 sec

Fig. 8. (Contd.)

to a degree (Fincham and Spedding 1997), the filtering is still less efficient locally compared with the inside region where sufficient number of vectors are available in all directions.

Figure 6c shows similar energy spectra for the lateral velocity component, v, at $x = y = 0$. As expected, the energy spectra show neither orbital nor its harmonic frequencies in the lateral direction since the phase-averaged v is approximately zero and independent of the orbital frequency. Again, the turbulence spectral frequency range is

significantly extended from 10 Hz to 45 Hz and 60 Hz by the spatial and temporal post-processing, respectively.

Figure 7 shows energy spectra for $u^2(t)$, $v^2(t)$, $u'^2(t)$ and $v'^2(t)$ for the temporally post-processed data for all 60 waves. Unlike $u^2(t)$ spectra, the orbital frequency does not appear for $u'^2(t)$ since by definition $u'(t)$ carries only non-orbital fluctuation components. Indeed, for the range of frequencies higher than 5 Hz, with the orbital characteristics diminished, both spectra of $u^2(t)$ and $u'^2(t)$ collapse into almost a single characteristic. The energy spectra of $v(t)$ and $v'(t)$ conform to a nearly single characteristic for the whole frequency range, since there exist no prominent orbital or

harmonic frequencies in the lateral direction. The lower turbulence spectral frequency range measured for $u^2(t)$ and $u'^2(t)$, 30 Hz, compared with 60 Hz for $v^2(t)$ and $v'^2(t)$, may be explained by "aliasing" in that the direction of the flow vector is oblique to the of measurement. The presence of aliasing tends to measure a lower frequency than the actual one because of the skewness, and more aliasing is expected to occur in the longitudinal direction since the longitudinal flow carries a higher degree of freedom than the lateral flow in such a long wave flume.

546

3.4
Velocity, vorticity, and acceleration field mapping

Figure 8a shows sequential images of instantaneous velocity vector fields at the measurement plane 2 cm above the bottom in arrows and corresponding cut-through vorticity, $\omega_z = \partial v/\partial x - \partial u/\partial y$, in isotherm contours. Note that the first three images are presented in 4-ms intervals, the next three images in 20-ms intervals, and the last three images in 40-ms intervals. The overall time span from 0.52 s to 0.72 s roughly corresponds to the period from the wave breaking to the descending eddies reaching the bottom.

Stoke's theorem states that the average vortex within a closed area is equal to the circulation integrated along the boundary divided by the total area, i.e.,

$$\varpi_z = \frac{1}{A} \oint_S (u\mathrm{d}x + v\mathrm{d}y) \tag{6}$$

By choosing a rectangular area of $2\Delta_x \times 2\Delta_y$ (Fig. 9), which connects the centers of eight grids ($\Delta_x = \Delta_y = 2.21$ mm with 50% overlapping), the local circulation is formulated as:

$$\oint u\mathrm{d}x = \frac{1}{2}\left(u_{i-1,j-1} + 2u_{i,j-1} + u_{i+1,j-1}\right)\Delta_x$$
$$- \frac{1}{2}\left(u_{i+1,j+1} + 2u_{i,j+1} + u_{i-1,j+1}\right)\Delta_x$$
$$\oint v\mathrm{d}y = \frac{1}{2}\left(v_{i+1,j-1} + 2v_{i+1,j} + v_{i+1,j+1}\right)\Delta_y \tag{7}$$
$$- \frac{1}{2}\left(v_{i-1,j+1} + 2v_{i-1,j} + v_{i-1,j-1}\right)\Delta_y$$
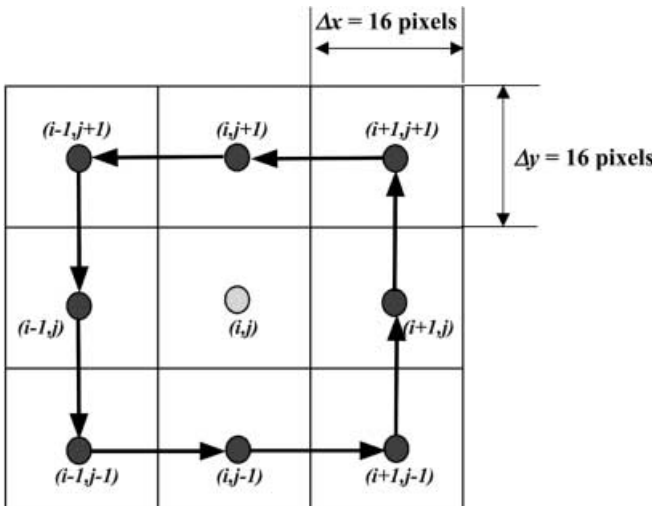$$A = 4\Delta_x\Delta_y$$

Fig. 9. Local circulation method for vorticity estimation at (i, j)

Selected contours of two-dimensional cut-through vorticity isotherms shown in Fig. 8a identify regions of highly rotational range of $|\omega_z| \geq 18\,\mathrm{s}^{-1}$. The vortex structure initially at the left-hand side propagates into the center of the plane and the vortex size and strength varies with its propagation.

The phase-averaged velocity fields at the same measurement plane as in Fig. 8a, for the 60 repeating waves, are shown in Fig. 8b. While the instantaneous fields show dramatically rotational and randomly occurring flows, the phase-averaged fields deviate little from largely reciprocating movement at the wave generation frequency of 0.5 Hz.

For the same condition, temporal evolution of the two-dimensional acceleration field is shown in Fig. 10a. Though the descending eddy flow is three-dimensional in general, the relatively planar flow near the bottom surface is assumed approximately two-dimensional. The x-component Navier–Stokes equation describing a two-dimensional flow of incompressible fluid is written as:

$$\rho a_x(x,y,t) = \rho \frac{\mathrm{D}u(x,y,t)}{\mathrm{D}t} = \rho g - \frac{\partial p(x,y,t)}{\partial x}$$
$$+ \mu\left(\frac{\partial^2 u(x,y,t)}{\partial x^2} + \frac{\partial^2 u(x,y,t)}{\partial y^2}\right) \tag{8}$$
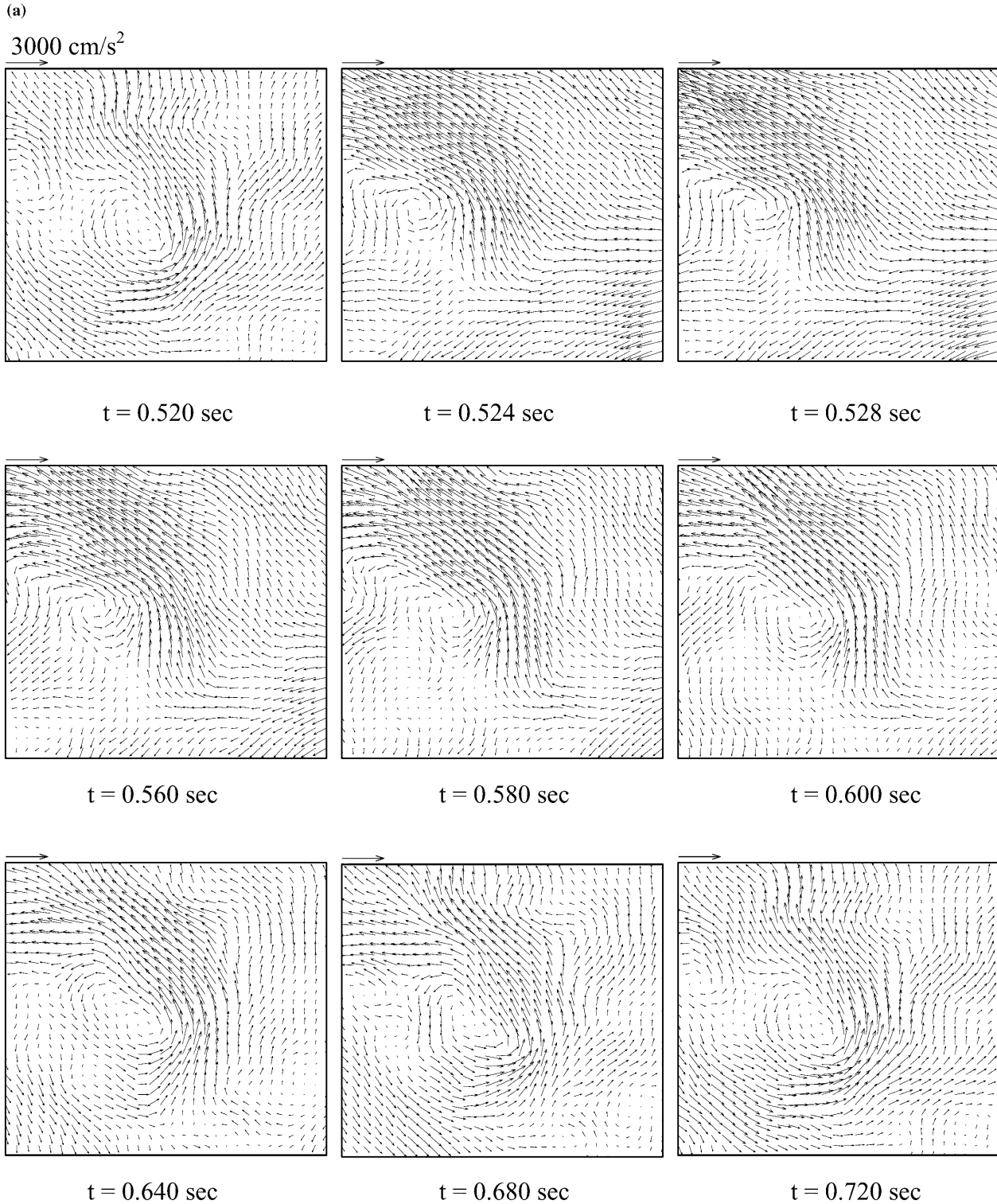
where the body force term remains constant for the present case. The frictional term can be calculated by numerical differentiation of the velocity vector field experimentally obtained with spatial and temporal resolution. Then, the pressure $p(x,y,t)$ can be determined once the acceleration field is calculated from the measured cinematographic velocity vector field.

The finite difference formulation gives the Eulerian acceleration by a modified formula using an analysis similar to Jacobsen et al. (1997):

$$\frac{\mathrm{D}u(x_o,y_o,t_o)}{\mathrm{D}t}$$
$$= \frac{\partial u}{\partial t} + u\frac{\partial u}{\partial x} + v\frac{\partial u}{\partial y}$$
$$= \frac{1}{2}\left[\frac{u(x_o,y_o,t_+) - u(x_o,y_o,t_o)}{\Delta_t} + \frac{u(x_o,y_o,t_o) - u(x_o,y_o,t_-)}{\Delta_t}\right]$$
$$+ \frac{1}{2}\left[\begin{array}{l} u(x_o,y_o,t_o)\frac{u(x_+,y_o,t_o)-u(x_o,y_o,t_o)}{\Delta_x} + u(x_o,y_o,t_o)\frac{u(x_o,y_o,t_o)-u(x_-,y_o,t_o)}{\Delta_x} \\ + v(x_o,y_o,t_o)\frac{u(x_o,y_+,t_o)-u(x_o,y_o,t_o)}{\Delta_y} + v(x_o,y_o,t_o)\frac{u(x_o,y_o,t_o)-u(x_o,y_{-1},t_o)}{\Delta_y} \end{array}\right] \tag{9}$$

where the subscripts o, +, − for t denote the present, 4 ms ($\equiv \Delta_t$) after, and 4 ms before the present occurring, respectively. For x and y, the same three subscripts denote the center, 2.21 mm (Δ_x or Δ_y with 50% overlapping) positive, and 2.21 mm negative locations with respect to the center, respectively. The circular acceleration decreases as the vortex propagates and dissipates with the flow. Also, the overall flow is shown to decelerate with the vortex propagation. The phase-averaged acceleration fields for the same time span are shown in Fig. 10b. Similar to the phase-averaged velocity fields, the phase-averaged acceleration is largely reciprocating at the wave frequency of 0.5 Hz.

The full-field data can be readily converted to local flow data at any specified location within the imaging plane.

(a)

3000 cm/s^2

t = 0.520 sec   t = 0.524 sec   t = 0.528 sec

t = 0.560 sec   t = 0.580 sec   t = 0.600 sec

t = 0.640 sec   t = 0.680 sec   t = 0.720 sec

Fig. 10. a Temporal development of instantaneous acceleration field surrounding the descending eddies, detected at 2 cm above the bottom of the surf zone. **b** Temporal development of phase-averaged acceleration field from 60 waves and cut-through vorticity contours at 2 cm above the bottom of the surf zone

Figure 11 shows an example of instantaneous (dashed lines) and phase-averaged (solid lines) data sampled at the center of the measurement plane, $u(0, 0, t)$, $v(0, 0, t)$, $k(0, 0, t)$, and $|u'\ v'|$ $(0, 0, t)$. The instantaneous data describe the same wave as in Figs. 8 and 10. Both instantaneous u and v show significant fluctuations from their phase-averaged values. The turbulence kinetic energy and the magnitude of turbulence shear stress are shown in Fig. 11c and d, respectively. Since the present measurement is limited for two-dimensional sampling, the turbulence kinetic energy is based on the x and y components, i.e., $k = (u'^2 \pm v'^2)/2$, and the shear stress presents only a
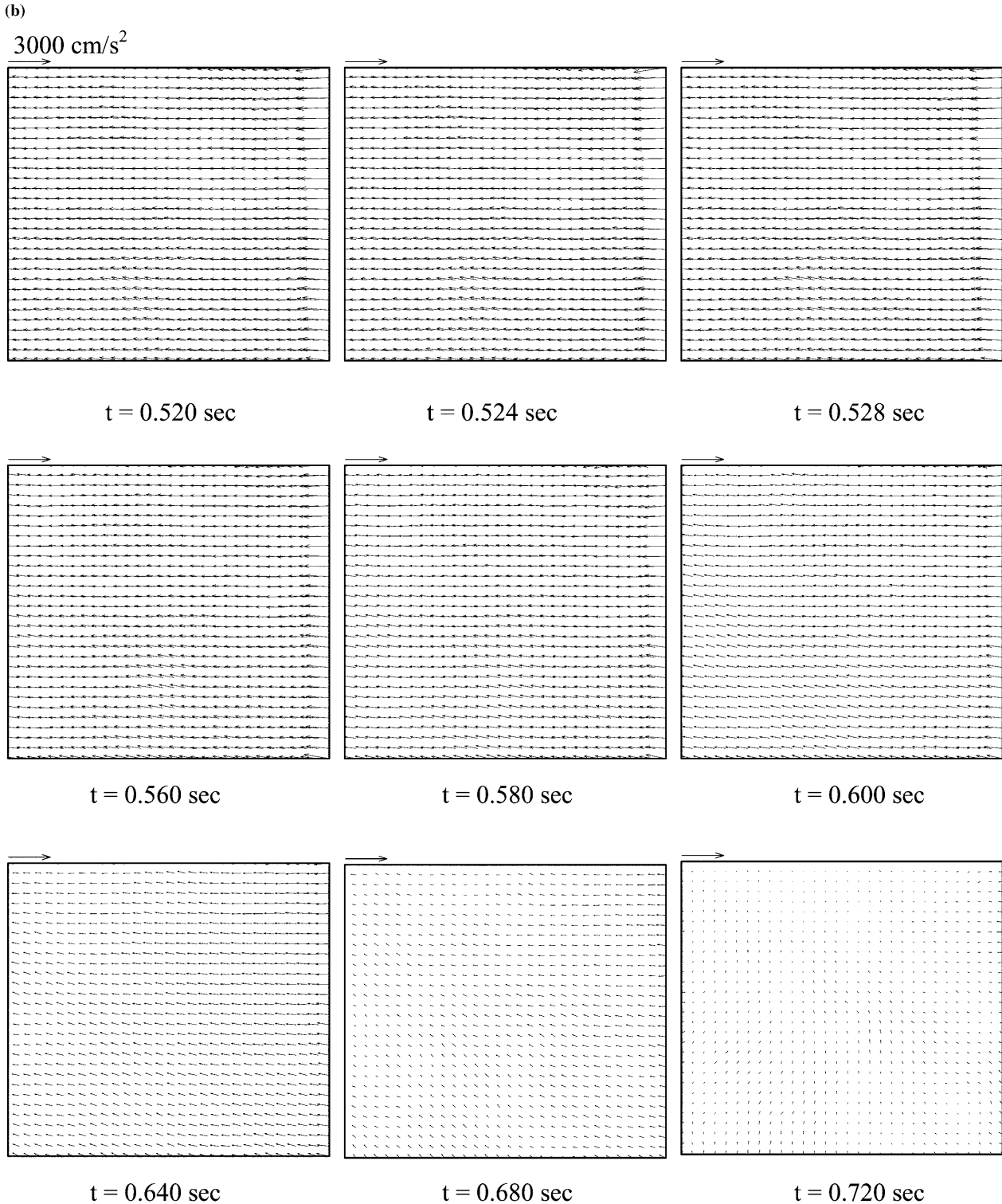
(b)

3000 cm/s²

t = 0.520 sec   t = 0.524 sec   t = 0.528 sec

t = 0.560 sec   t = 0.580 sec   t = 0.600 sec

t = 0.640 sec   t = 0.680 sec   t = 0.720 sec

548

Fig. 10. (Contd.)

single component of $|u'v'|$. Both turbulence kinetic energy and turbulence shear stress show stronger fluctuations for the highly fluctuating period from 0.52 s to 0.72 s.

4
Conclusion

The use of a pulsed copper-vapor laser source, synchronized with a high-speed CCD camera, has developed a digital cinematographic PIV system. The system has exhibited a feasibility to measure temporal and spatial turbulent properties of transient and non-periodic flows, such as in the surf-zone bottom shear layer that is created by descending eddies from the surface wave break. Combined use of the spatial median filtering and the temporal median filtering can significantly improve the vector validation compared with the use of only the conventional spatial filtering. With an assumption of two-dimensional flows, a temporal history of full-field cut-through vorticity distribution has been
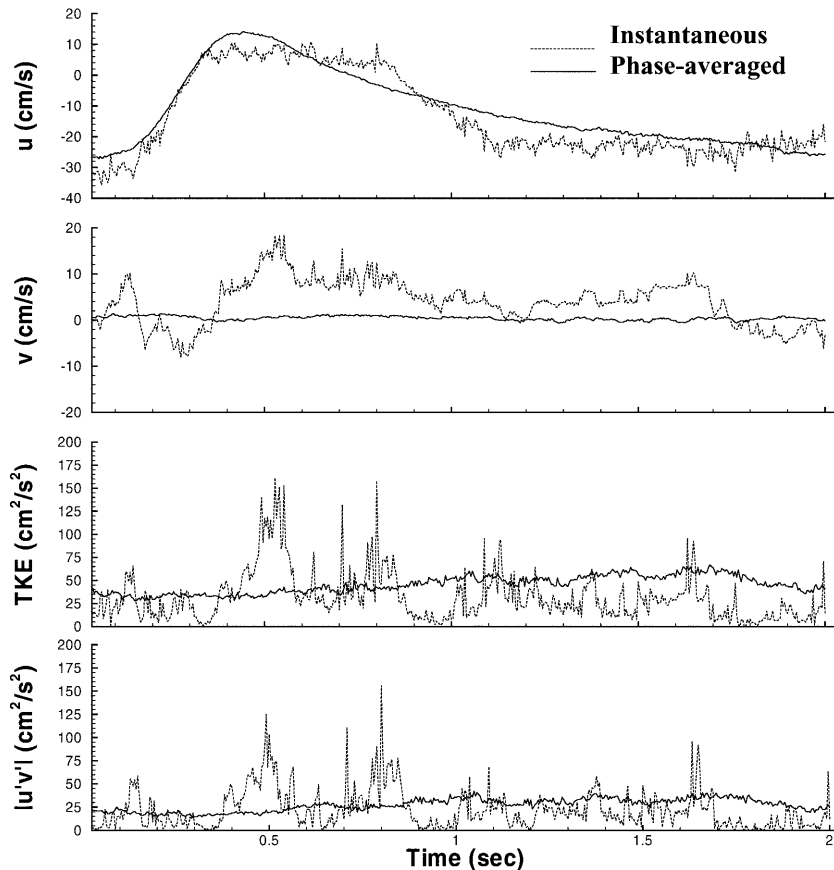
Fig. 11. Temporal history of instantaneous and phase-averaged data for the whole wave period sampled at $x = y = 0$ in the plane 2 cm above the bottom

mapped, which would not be possible by point-probes or intermittently sampled PIV measurements. From the cinematographic data, instantaneous and phase-averaged properties are also available at any point in the measurement plane and at any instant during the wave period.

References

Adrian RJ (1986) An image shifting technique to resolve directional ambiguity in double-pulsed velocimetry: Appl Opt 25: 3855–3858

Adrian RJ (1996) Bibliography of particle image velocimetry using imaging methods: 1917–1995. TAM Report 817, UILU-ENG-96-6004, University of Illinois (available from fluid@tsi.com)

Adrian RJ (1997) Dynamic ranges of velocity and spatial resolution of particle image velocimetry: Meas Sci Technol 8: 1393–1398

Bradshaw P (1971) An introduction to turbulence and its measurement. Pergamon Press, Oxford, p 152

Fincham AM; Spedding GR (1997) Low cost, high resolution DPIV for measurement of turbulent fluid flow. Exp Fluids 23: 449–462

Goodman JW (1996) Introduction to Fourier optics. McGraw-Hill, San Francisco

Gray C; Greated CA; McCluskey DR; Easson WJ (1991) An analysis of the scanning beam PIV illumination system. Meas Sci Technol 2: 717–724

Gui LC; Merzkirch W (1996) A method of tracking ensembles of particle images. Exp Fluids 21: 465–468

Hartmann J; Köhler; Stolz W; Flögel (1996) Evaluation of transient flow fields using cross-correlation in image sequences. Exp Fluids 20: 210–217

Hassan YA; Philip OG; Schmidl WD (1993) Bubble collapse velocity measurements using a PIV technique with fluorescent tracers. ASME FED vol. 172: 85–92

Jakobsen ML; Dewhirst TP; Greated CA (1997) Particle image velocimetry for predictions of acceleration fields and force within fluid flows. Meas Sci Technol 8: 1502–1516

Keane RD; Adrian RJ (1992) Theory of cross-correlation analysis of PIV images. Appl Sci Res 49: 191–215

Lawson NJ; Rudman M; Guerra A; Liow J-L (1999) Experimental and numerical comparisons of the break-up of a large bubble. Exp Fluids 26: 524–534

Lee SD; Chung SH; Kihm KD (1996) Suggestive correctional methods for PIV image biasing caused by a rotating mirror system. Exp Fluids 21: 202–208

Lin JC; Rockwell D (1995) Evolution of a quasi-steady breaking wave. J Fluid Mech 302: 29–44

Liu S; Katz J; Meneveau C (1999) Evolution and modeling of subgrid scales during rapid straining of turbulence. J Fluid Mech 387: 281–320

Lyn DA (1997) A PIV study of an oscillating-grid flow. ASME Fluids Engineering Division Summer Meeting. FEDSM97-3060

Merzkirch W; Mrosewski T; Wintrich H (1994) Digital particle image velocimetry applied to a natural convective flow. Acta Mech 4: 19–26

Nadaoka K; Hino M; Koyano Y (1989) Structure of the turbulent flow field under breaking waves in the surf zone. J Fluid Mech 204: 359–387

Oakley TR; Loth E; Adrian RJ (1997) A two-phase cinematic PIV method for bubbly flows. J Fluid Eng 119: 707–712

Raffel M; Kompenhans J (1995) Theoretical and experimental aspects of image-shifting by means of a rotating mirror system for particle image velocimetry. Meas Sci Technol 6: 795–808

Raffel M; Seelhorst U; Willert C; Vollmers H; Bütefisch KA; Kompenhans J (1996) Measurement of vortical structures on a

helicopter rotor model in a wind tunnel by LDV and PIV. In: Proceedings of the 8th International Symposium on Applications of Laser Techniques to Fluid Mechanics, Instituto Superior Técnico, Lisbon, Portugal, p 14-3

Raffel M; Willert C; Kompenhans J (1998) Particle image velocimetry. Springer, Berlin Heidelberg New York

She K; Greated CA; Easson WJ (1997) Experimental study of three-dimensional breaking wave kinematics. Appl Ocean Res 19: 329–343

Son SY; Kihm KD; Sohn DK; Jang YJ; Han J-C (1999) Coolant flow field measurements in a two-pass channel using PIV. J Heat Trans (Heat Transfer Gallery – Special Insert) 121: 3

Tennekes H; Lumley JL (1972) A first course in turbulence. MIT Press, Cambridge, Mass.

Tokuhiro A; Fujiwara A; Hishida K; Maeda M (1999) Measurement in the wake region of two bubbles in close proximity by combined shadow-image and PIV techniques. J Fluid Eng 121: 191–197

Westerweel J (1994) Efficient detection of spurious vectors in PIV data. Exp Fluids 16: 236–247

Westerweel J; Dabiri D; Gharib M (1997) The effect of a discrete window offset on the accuracy of cross-correlation analysis of digital PIV recordings. Exp Fluids 23: 20–28